2015

Model-based correction for scatter and tailing effects in simultaneous 99mTc and 123I imaging for a CdZnTe cardiac SPECT camera

Maria Holstensson
University College London

Kjell Erlandsson
University College London

Gavin Poludniowski
Karolinska University Hospital

Simona Ben-Haim
University College London

Brian F. Hutton
University of Wollongong, University College London

Model-based correction for scatter and tailing effects in simultaneous 99mTc and 123I imaging for a CdZnTe cardiac SPECT camera

Abstract

2015 Institute of Physics and Engineering in Medicine. An advantage of semiconductor-based dedicated cardiac single photon emission computed tomography (SPECT) cameras when compared to conventional Anger cameras is superior energy resolution. This provides the potential for improved separation of the photopeaks in dual radionuclide imaging, such as combined use of ^{99m}Tc and ^{123}I . There is, however, the added complexity of tailing effects in the detectors that must be accounted for. In this paper we present a model-based correction algorithm which extracts the useful primary counts of ^{99m}Tc and ^{123}I from projection data. Equations describing the in-patient scatter and tailing effects in the detectors are iteratively solved for both radionuclides simultaneously using a maximum a posteriori probability algorithm with one-step-late evaluation. Energy window-dependent parameters for the equations describing in-patient scatter are estimated using Monte Carlo simulations. Parameters for the equations describing tailing effects are estimated using virtually scatter-free experimental measurements on a dedicated cardiac SPECT camera with CdZnTe-detectors. When applied to a phantom study with both ^{99m}Tc and ^{123}I, results show that the estimated spatial distribution of events from ^{99m}Tc in the ^{99m}Tc photopeak energy window is very similar to that measured in a single ^{99m}Tc phantom study. The extracted images of primary events display increased cold lesion contrasts for both ^{99m}Tc and ^{123}I.

Keywords

imaging, cdznte, cardiac, spect, camera, scatter, model, tailing, correction, effects, simultaneous, 123i, 99mtc

Disciplines

Engineering | Science and Technology Studies

Model-based correction for scatter and tailing effects in simultaneous ^{99m}Tc and ^{123}I imaging for a CdZnTe cardiac SPECT camera

Model-based correction for scatter and tailing effects in simultaneous ^{99m}Tc and ^{123}I imaging for a CdZnTe cardiac SPECT camera

M Holstensson[1,2]**, K Erlandsson**[1]**, G Poludniowski**[3]**,
S Ben-Haim**[1,4]**, B F Hutton**[1,5]

[1] Institute of Nuclear Medicine, University College London, London, NW1 2BU, UK
[2] Department of Nuclear Medicine, Karolinska University Hospital, SE-141 86, Stockholm, Sweden
[3] Department of Medical Physics, Karolinska University Hospital, S-171 76 Stockholm, Sweden
[4] Department of Nuclear Medicine, Chaim Sheba Medical Center, Tel Hashomer, Ramat Gan 52621, Israel
[5] Centre for Medical Radiation Physics, University of Wollongong, NSW, Australia

E-mail: maria.holstensson@karolinska.se

CrossMark

Abstract

An advantage of semiconductor-based dedicated cardiac single photon emission computed tomography (SPECT) cameras when compared to conventional Anger cameras is superior energy resolution. This provides the potential for improved separation of the photopeaks in dual radionuclide imaging, such as combined use of ^{99m}Tc and ^{123}I . There is, however, the added complexity of tailing effects in the detectors that must be accounted for. In this paper we present a model-based correction algorithm which extracts the useful primary counts of ^{99m}Tc and ^{123}I from projection data. Equations describing the in-patient scatter and tailing effects in the detectors are iteratively solved for both radionuclides simultaneously using a maximum a posteriori probability algorithm with one-step-late evaluation. Energy window-dependent parameters for the equations describing in-patient scatter are estimated using Monte Carlo simulations. Parameters for the equations describing tailing effects are estimated using virtually scatter-free experimental measurements on a dedicated cardiac SPECT camera with CdZnTe-detectors. When applied to a phantom study with both ^{99m}Tc and ^{123}I, results show that the estimated spatial distribution of events from ^{99m}Tc in the ^{99m}Tc photopeak energy window is very similar to that measured in a

single ^{99m}Tc phantom study. The extracted images of primary events display increased cold lesion contrasts for both ^{99m}Tc and ^{123}I.

Keywords: CdZnTe, tailing effects, incomplete charge collection, dual radionuclide imaging, D-SPECT

(Some figures may appear in colour only in the online journal)

1. Introduction

Simultaneous imaging of ^{123}I- and ^{99m}Tc-labelled radiopharmaceuticals can be useful in a number of situations. The ^{99m}Tc-labelled radiopharmaceuticals sestamibi (MIBI) and tetrofosmin are commonly used for myocardial perfusion imaging (Baggish and Boucher 2008). The ^{123}I-labelled agents metaiodobenzylguanidine (MIBG) and iodophenylpentadecanoic acid (IPPA) can be used to image myocardial sympathetic innervation and fatty acid metabolism respectively (Verani *et al* 2000, Chirumamilla and Travin 2011). The use of combinations of these or other ^{99m}Tc- and ^{123}I-labelled agents can be advantageous as differences in uptake can assist in patient diagnosis. One example is imaging using the fatty acid analogue β-methyl-iodo-phenyl pentadecanoic acid (BMIPP) in conjunction with ^{99m}Tc-sestamibi perfusion imaging, where a mismatch is frequent in areas with acute myocardial infarction (De Geeter *et al* 1994, Kumita *et al* 2000). Another example is imaging using ^{99m}Tc-MIBI in conjunction with ^{123}I-MIBG where regions of mismatch were identified extending beyond perfusion defects (Ben-Haim *et al* 2014). ^{123}I-MIBG has been used sequential to ^{99m}Tc-tetrofosmin to assess transmyocardial laser revascularization (Muxi *et al* 2003). Studies of other parts of the body include parathyroid imaging employing simultaneous use of ^{123}I and ^{99m}Tc-sestamibi (Hindié *et al* 1998) and brain imaging employing simultaneous use of ^{99m}Tc-ECD and ^{123}I-FP-CIT (El Fakhri *et al* 2006).

Simultaneous imaging in these cases is preferable to sequential imaging as it reduces time spent on the camera which is beneficial to both the patient and the clinic. Simultaneously acquired images will also automatically be perfectly registered as opposed to ones acquired sequentially where image registration may be necessary. With a typical energy resolution of 10% for an Anger camera with a sodium iodide crystal, the close proximity of the two photopeaks of ^{99m}Tc and ^{123}I, at 140.5 keV and 159 keV respectively, results in cross-contamination between the photopeaks (also known as cross-talk between photopeaks). Suggested methods for simultaneous imaging in these cases include using an asymmetrical energy window for the ^{123}I photopeak (Devous *et al* 1992). This, however, reduces the counting efficiency for ^{123}I compared to using a symmetrical energy window (Ivanovic and Weber 1994). Other suggested methods for cross-contamination correction in dual radionuclide imaging using Anger cameras include model-based compensation (Kadrmas *et al* 1999), a rotation-based Monte Carlo simulation method (de Jong and Beekman 2000), constrained spectral factor analysis (El Fakhri *et al* 2000), the use of artificial neural networks (El Fakhri *et al* 2000, 2001, 2002, Zheng *et al* 2004), iterative generalised spectral factor analysis (Hapdey *et al* 2006), generalized five-dimensional dynamic and spectral factor analysis (El Fakhri *et al* 2006b), the Monte Carlo based joint iterative reconstruction algorithm (Ouyang *et al* 2007, 2009) and the analytical photon distribution algorithm (Shcherbinin *et al* 2009).

Two dedicated cardiac cameras based on CdZnTe semiconductor technology have now been made available by manufacturers: the D-SPECT (Spectrum Dynamics, Caesarea, Israel) and Discovery NM 530c (GE Healthcare, Milwaukee, US). When semiconductor detectors

are considered, one of the benefits is the superior energy resolution which assists in better separation of the two photopeaks. An additional benefit is that of superior sensitivity, allowing for dynamic tracer studies or low dose imaging protocols (Gimelli *et al* 2012, Ben-Haim *et al* 2013, Nakazato *et al* 2013). There is, however, a characteristic 'tailing effect' in the energy spectrum towards lower energies due to incomplete charge collection (Leo 1994). This effect and the pixelated design of dedicated cardiac cameras need to be considered when in-patient scatter and cross-contamination between the photopeaks is to be corrected for. Kacperski *et al* (2011) has proposed and validated a model-based correction algorithm for dual radionuclide imaging using ^{99m}Tc and ^{201}Tl for the D-SPECT dedicated cardiac camera with pixelated CdZnTe-detectors. The method employs multiple energy windows and model equations describing the tailing effects and scatter. The useful primary counts of the photopeaks are estimated by iteratively solving the equations using the acquired images in the energy windows. Monte Carlo simulations of point sources are employed to estimate the parameters for scatter modelling and experimental measurements using rod sources are employed to estimate the parameters for modelling of tailing effects.

In this paper we modify the model-based correction algorithm proposed by Kacperski *et al* (2011) and apply it to the new case of dual radionuclide imaging with ^{99m}Tc and ^{123}I . Monte Carlo simulations of digital chest phantoms are used in combination with experimental measurement using capillary tubes to estimate the appropriate parameters to be implemented in the algorithm. The equations are iteratively solved to extract the primary events from ^{99m}Tc- and ^{123}I-images acquired simultaneously.

2. Methods

The proposed correction algorithm seeks to iteratively estimate the primary and scatter components of ^{99m}Tc and ^{123}I by solving a set of equations, utilising models describing both tailing effects and scatter. The method employs multiple energy windows which are defined in section 2.1.1. The modelling of tailing effects which utilises parameters estimated using scatter-free experimental measurements is described in section 2.2. The modelling of photopeak scatter which utilises parameters estimated using Monte Carlo simulations is described in section 2.3. Scattered events from higher energy emissions of ^{123}I are treated separately which is described in section 2.3.2 and the full set of equations to be solved is presented in section 2.4. A priori knowledge regarding the scatter fractions of ^{99m}Tc and ^{123}I used to aid convergence is described in section 2.4.1. Three experimental phantom studies, described in section 2.5, were performed in order to evaluate the proposed correction algorithm.

2.1. Simultaneous imaging using ^{123}I and ^{99m}Tc on the D-SPECT

A schematic drawing of the D-SPECT geometry can be seen in figure 1. Nine detectors are arranged in an arc around the chest of the patient. Each detector is composed of a 16 × 64 CdZnTe pixel array (16 in the transaxial direction and 64 in the axial direction) with a pixel pitch of 2.46 mm. Each detector is equipped with a parallel square hole tungsten collimator with a hole centre separation of 2.46 mm, centred over the individual pixels, and a septal thickness of 0.2 mm. During a SPECT scan the detectors rotate around their own individual central axes (sweep mode) and are translated to ensure complete tomographic sampling. Additional time is spent on the region of the heart which is determined in a scout scan prior to the full SPECT acquisition (Erlandsson *et al* 2009). All D-SPECT scans are acquired in list mode which allows for images to be generated for any number of energy windows post acquisition.
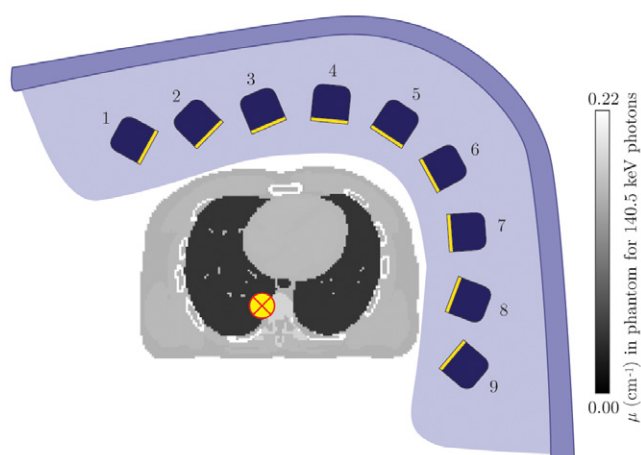
Figure 1. Schematic drawing of the D-SPECT geometry together with a transaxial slice of the default male XCAT attenuation coefficient (μ for 140.5 keV photons) phantom. The positions of the nine detectors, directed at the centre of the heart, are indicated with numbers. During a SPECT acquisition each detector rotates around its own axis in order to cover the whole field of view. The position for capillary tubes for measurements described in section 2.2 is marked with a cross.
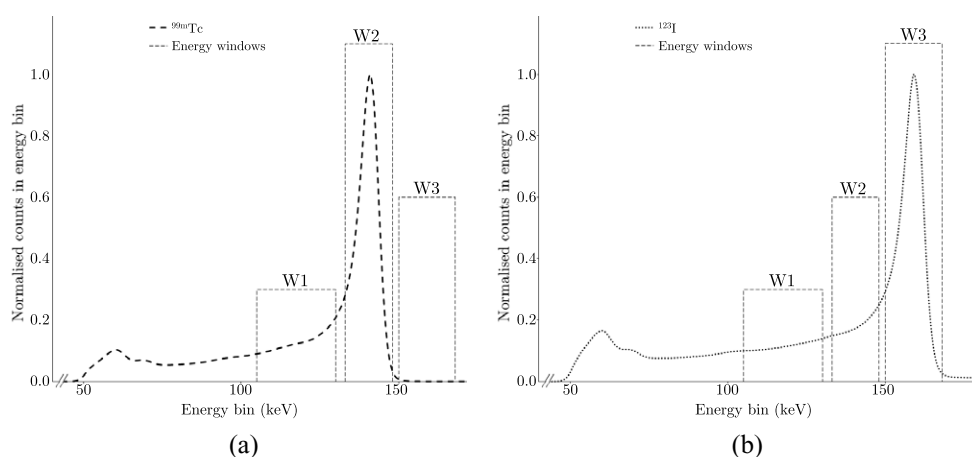
Figure 2. Experimentally measured energy spectra using capillary tubes filled with (*a*) ^{99m}Tc and (*b*) ^{123}I. The tailing effect of incomplete charge collection at energies below the photopeak is evident.

2.1.1. Energy windows. Two energy spectra experimentally measured on the D-SPECT system using capillary tubes filled with ^{99m}Tc and ^{123}I are presented in figure 2(*a*) and (*b*) respectively. The capillary tubes result in virtually scatter-free sources. The energy windows covering the photopeaks can be seen in the figure: W2 covers the ^{99m}Tc photopeak at 140.5 keV (133–148 keV) and W3 covers the ^{123}I photopeak at 159 keV (150–168 keV). It can be observed from these energy spectra that the contribution from ^{99m}Tc counts in W3 is negligible. The tailing effect of incomplete charge collection at energies below the photopeak, evident in these figures, is discussed in section 2.2. Figure 3 shows two energy spectra in units of counts per
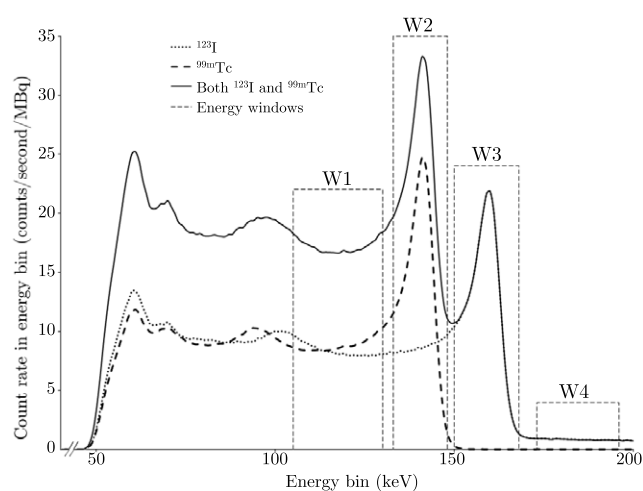
Figure 3. Two separately measured energy spectra using an anthropomorphic phantom with a cardiac insert filled with ^{123}I and ^{99m}Tc. The summed energy spectrum and the energy windows used in this study are also shown.
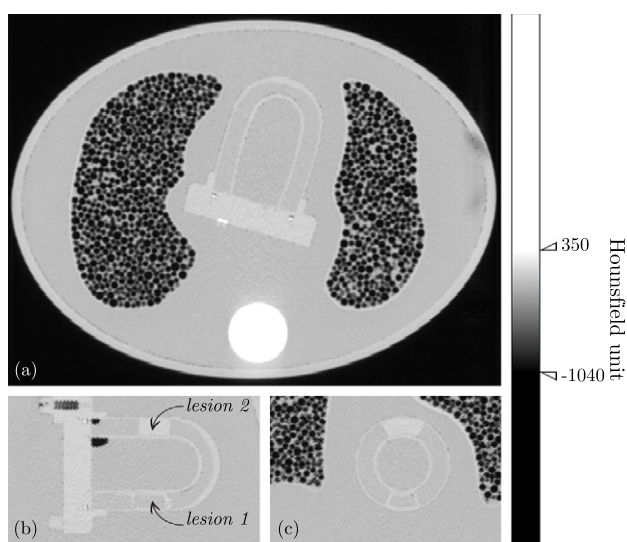
Figure 4. A transaxial slice from a CT scan of the anthropomorphic phantom (*a*), vertical long axis of the cardiac insert (*b*) and short axis of the cardiac insert (*c*). The two lesions in the cardiac insert are indicated.

second per MBq separately measured using ^{99m}Tc and ^{123}I in the anthropomorphic phantom with scattering material shown in figure 4. The activity distribution in the phantom is specified in section 2.5. The summed energy spectrum of the two is shown as are two additional energy windows. W1 (105–130 keV) is situated below both photopeaks and is used in the count model as a window receiving scattered events and tailing effects from both photopeaks. W4 (173–196 keV) is situated above both photopeaks and is used to estimate the scattered events from ^{123}I-emissions with energies higher than 159 keV (NNDC 2000).

2.2. Modelling of tailing effects

A characteristic effect of impurities in irregularities in the CdZnTe-crystal lattice is that of trapping of electrons or holes (Leo 1994). When the trapping time is longer than the charge collection time this results in incomplete charge collection of photon detection. Tailing effects can also occur when a fraction of the photopeak signal is detected in one pixel and another fraction in a neighbouring pixel due to either charge cloud overlap (also known as cross-talk between pixels) or Compton and/or x-ray fluorescent scattering (Wagenaar 2004). The characteristic tailing effect of incomplete charge collection is evident in figure 2.

The model which describes the distribution of tailing photopeak events in an energy window below the photopeak energy window ($P_{\mathrm{ph} \rightarrow \mathrm{lo}}$) can be described by equation (1) (Kacperski *et al* 2011)

$$P_{\mathrm{ph} \rightarrow \mathrm{lo}} = w_{\mathrm{ph} \rightarrow \mathrm{lo}} \cdot P_{\mathrm{ph}} \bigotimes K^{P}_{\mathrm{ph} \rightarrow \mathrm{lo}} \tag{1}$$

where ph indicates the photopeak energy window, lo indicates the lower energy window, $w_{\mathrm{ph} \rightarrow \mathrm{lo}}$ is a window-dependent weight factor and P_{ph} is the image of the primary events in the photopeak energy window. $K^{P}_{\mathrm{ph} \rightarrow \mathrm{lo}}$ is a Gaussian kernel characterised by the window-dependent value of $\sigma_{\mathrm{ph} \rightarrow \mathrm{lo}}$. The values of $w_{\mathrm{ph} \rightarrow \mathrm{lo}}$ and $\sigma_{\mathrm{ph} \rightarrow \mathrm{lo}}$ were estimated for all coupled energy windows using experimentally acquired projection images of capillary tubes filled with $^{99\mathrm{m}}$Tc and ^{123}I separately. The capillary sources were placed at the centre of the gantry (marked with a cross in figure 1) on a polystyrene block. The experimental setup is assumed to be scatter free and hence it is assumed that all events detected in ph are primary events and all events detected in lo are events from tailing effects. $w_{\mathrm{ph} \rightarrow \mathrm{lo}}$ was calculated as $N_{\mathrm{lo}}/N_{\mathrm{ph}}$ where N_{lo} and N_{ph} are the total number of counts in the photopeak and lower energy windows respectively. As the line-spread in the lower window is modelled as the line-spread in the photo-peak convolved with a Gaussian, it follow that: $\sigma_{\mathrm{ph} \rightarrow \mathrm{lo}} = \sqrt{\sigma_{\mathrm{lo}}^{2} - \sigma_{\mathrm{ph}}^{2}}$. σ_{lo} and σ_{ph} are the standard deviations of Gaussian fits to line profiles across the images of the capillary tubes for the photopeak and lower energy windows respectively. $w_{\mathrm{ph} \rightarrow \mathrm{lo}}$ and $\sigma_{\mathrm{ph} \rightarrow \mathrm{lo}}$ were estimated for all nine detectors separately and the average values were calculated.

2.3. Modelling of scatter

The model which describes the scatter in an energy window below the photopeak energy window ($S_{\mathrm{ph} \rightarrow \mathrm{lo}}$) can be described by equation (2) (Kacperski *et al* 2011)

$$S_{\mathrm{ph} \rightarrow \mathrm{lo}} = C_{\mathrm{ph} \rightarrow \mathrm{lo}} \cdot \left(S_{\mathrm{ph}} + \alpha_{\mathrm{ph} \rightarrow \mathrm{lo}} \cdot S_{\mathrm{ph}} \bigotimes K^{S}_{\mathrm{ph} \rightarrow \mathrm{lo}} \right) \tag{2}$$

$$K^{S}_{\mathrm{ph} \rightarrow \mathrm{lo}} = \mathrm{e}^{-\lambda_{\mathrm{ph} \rightarrow \mathrm{lo}} \cdot r} \tag{3}$$

where $C_{\mathrm{ph} \rightarrow \mathrm{lo}}$ and $\alpha_{\mathrm{ph} \rightarrow \mathrm{lo}}$ are window-dependent weight factors and S_{ph} is the image of the photopeak scatter events. The kernel $K^{S}_{\mathrm{ph} \rightarrow \mathrm{lo}}$, expressed in equation (3), is described by a mono-exponential function characterised by the window-dependent value of $\lambda_{\mathrm{ph} \rightarrow \mathrm{lo}}$ (r is the radial distance). This is similar to other models in the literature (e.g. Meikle *et al* (1991)). The values of $C_{\mathrm{ph} \rightarrow \mathrm{lo}}$, $\alpha_{\mathrm{ph} \rightarrow \mathrm{lo}}$ and $\lambda_{\mathrm{ph} \rightarrow \mathrm{lo}}$ were estimated using Monte Carlo simulations as described in section 2.3.1.

2.3.1. Monte Carlo modelling of photopeak scatter.

The contribution from scattered events in a photopeak window to energy windows below was modelled using the Monte Carlo software SIMIND (Ljungberg and Strand 1989). The software XCAT (Segars *et al* 2010) was used to

generate digital chest phantoms of the adult male with a uniform activity distribution in the heart muscle. The linear attenuation coefficient maps were generated for both 140.5 keV and 159 keV and simulated separately. A transaxial slice of the phantom can be seen in figure 1. The phantom matrices were of size $128 \times 128 \times 128$ with pixels of size 2.75 mm.

Nine simulations, representing the nine detectors of the D-SPECT, were set up for each radionuclide. The photons emitted from the heart will have been subjected to different tissue paths depending on which detectors they reach as seen in figure 1. Hence the fraction of scattered events detected will vary between the detectors. An in-house written MATLAB script was used to position the phantom in the D-SPECT geometry and the detectors were set to point to the centre of the left ventricle. A batch of nine simulations in total (one projection per detector head) was generated with the appropriate angle and distance between the phantom and each detector. A continuous detector was used in combination with a tungsten collimator with square holes of the same size as that of the D-SPECT and the appropriate values for the energy resolution of the CdZnTe-detector at 140.5 keV and 159 keV were used. More complex physics such as tailing effects in the detector were not included in order to isolate the relative effects of in-patient scatter in different energy windows. It should be noted that Monte Carlo modelling of CdZnTe-detectors in cardiac SPECT systems in SIMIND is in development (Ljunberg *et al* 2014) but not yet fully validated and was not available for this study. The higher energy emissions of ^{123}I were not included in the simulations as those are treated separately as explained in section 2.3.2. Image matrices of size 256×256 with pixels of size 2.46 mm were acquired in the energy windows W1, W2 and W3.

The resulting scatter images were used in an in-house written MATLAB script to estimate the parameters in equation (2). The scatter distribution in the photopeak window, S_{ph}, was used in a genetic algorithm (MATLAB 2013) to estimate which set of $C_{\mathrm{ph} \to \mathrm{lo}}$, $\alpha_{\mathrm{ph} \to \mathrm{lo}}$ and $\lambda_{\mathrm{ph} \to \mathrm{lo}}$ yielded images with the minimised mean of the square differences between $S_{\mathrm{ph} \to \mathrm{lo}}$ and the 'true' scatter image in lo as given by the Monte Carlo simulations. The images of all nine detectors were used simultaneously in the optimisation algorithm, generating a global depth-averaged estimate of the best parameters to be used.

2.3.2. Scatter from higher energy emissions.

In addition to the scatter originating from the photopeak at 159 keV when imaging ^{123}I there is also a low level contribution from multiple high energy emissions. The contribution from these events to lower energy windows ($S_{W4 \to lo}$) was assumed constant and estimated using equation (4)

$$S_{W4 \to \mathrm{lo}} = S_{\mathrm{W4}} \cdot \Delta E_{\mathrm{lo}} / \Delta E_{\mathrm{W4}}, \tag{4}$$

where S_{W4} is the directly measured image in energy window W4. This window is assumed to only contain scattered events from higher energy emissions of ^{123}I . ΔE_{W4} and ΔE_{lo} are the widths of energy window W4 and the lower energy window respectively. This is a very similar approach to the two-window method applied by Kobayashi *et al* (2003).

2.4. Equations to Be solved

The images of all events in energy windows W1, W2 and W3 are denoted A_{W1}, A_{W2} and A_{W3} respectively and are given by equations (5a)–(5c).

$$A_{\mathrm{W1}} = P_{\mathrm{W2} \to \mathrm{w1}} + S_{\mathrm{W2} \to \mathrm{w1}} + P_{\mathrm{W3} \to \mathrm{w1}} + S_{\mathrm{W3} \to \mathrm{w1}} + S_{W4 \to w1} \tag{5a}$$

$$A_{\mathrm{W2}} = P_{\mathrm{W2}} + S_{\mathrm{W2}} + P_{\mathrm{W3} \to \mathrm{w2}} + S_{\mathrm{W3} \to \mathrm{w2}} + S_{W4 \to \mathrm{w2}} \tag{5b}$$

$$A_{\mathrm{W3}} = P_{\mathrm{W3}} + S_{\mathrm{W3}} + S_{W4 \to w3} \tag{5c}$$

We seek to extract the unknown primary components for the two photopeaks: P_{W2} for ^{99m}Tc and P_{W3} for ^{123}I. These images represent the activity distribution in the patient or phantom free from scattered events and tailing effects. In order to do so we need to also estimate the unknown self-scatter (the scatter from the photopeak in its own energy window) for the two photopeaks (S_{W2} and S_{W3}) and solve the linear problems described by equations (1) and (2) as we take the forward models described by equations (4) and (5*a*)–(5*c*) into consideration. The equations could in principle be solved using the maximum-likelihood expectation-maximisation (ML-EM) algorithm, as in Kacperski *et al* (2011). However, we found that, in this case, it was necessary to utilise a priori knowledge regarding the scatter fractions of ^{99m}Tc and ^{123}I, in order to aid convergence. Therefore, we opted for a maximum a posteriori probability (MAP) algorithm with one-step-late (OSL) evaluation (Green 1990). This approach is described in section 2.4.1. Note that in the approach presented by Kacperski *et al* (2011) the estimation of the scatter components was used in combination with the triple energy window scatter correction approach (Ogawa *et al* 1991). The approach presented here directly estimates the scatter components in each energy window.

The algorithm was initialised with the guesses that P_{W3} and S_{W3} were 80% and 20% respectively of the measured data in W3 and P_{W2} and S_{W2} were 40% and 10% respectively of the measured data in W2. The final converged solution is not sensitive to these starting values. However, the number of iterations required to reach the convergence do differ depending on the initial estimates.

At the stage in the algorithm where equation (2) is applied the estimates of S_{ph} are rebinned to obtain conventional planar projections before convolution with $K^S_{ph \to lo}$. The D-SPECT design consists of nine smaller detectors that are exposed to in-patient scatter from activity outside their direct field of view which this approach accounts for (Kacperski *et al* 2011). After the convolution step inverse rebinning is applied to obtain the original projection composition.

Due to imperfections in the crystal-growing process there is a variation in uniformity of response between pixels in cameras with CdZnTe-detectors which is easily corrected for using uniformity correction maps (Wagenaar 2004). In order to account for non-uniformity of the detectors, each component in equations (5*a*)–(5*c*) were multiplied by an appropriate experimentally measured uniformity map. This was a necessary step before comparison of the estimated and the measured images.

2.4.1. Constraint. To aid convergence a constraint was incorporated in the algorithm. A Monte Carlo study was performed to investigate the relationship between the detection of ^{99m}Tc and ^{123}I activity in the heart muscle. In a clinical study, the relative activity levels of ^{99m}Tc and ^{123}I are unknown. Also, the fraction of primary events will be dependent on the size of the patient. However, the photopeak emissions of the two radionuclides should be affected to similar degrees regardless of their relative activity levels in the heart muscle. Digital chest phantoms of the adult female with a uniform activity distribution in the heart muscle were generated using the XCAT software. Four different sizes of breast tissue were generated to simulate different size patients. The distances between the apex of the heart and the chest surface of the phantoms were 4 cm, 5 cm, 7 cm and 9 cm respectively. The phantom sizes are denoted 1–4 respectively with 1 being the smallest and 4 being the largest. The linear attenuation coefficient maps were generated for both 140.5 keV and 159 keV and simulated separately. The high energy emissions of ^{123}I were omitted in the simulations as only the photopeak scatter was to be taken into consideration. The phantom matrices were of size $128 \times 128 \times 128$ with pixels of size 2.75 mm. SIMIND was set up in the same way as described in section 2.3.1 and the detector was placed anterior to the phantoms at 17.6 cm distance from the centre of the

Table 1. Primary-to-scatter ratios (PTS) for different size phantoms for ^{99m}Tc and ^{123}I.

	Phantom size			
	1	2	3	4
PTS ^{99m}Tc (W2)	4.52	4.02	3.06	2.51
PTS ^{123}I (W3)	4.95	4.37	3.40	2.80
^{99m}Tc-to-^{123}I-ratio for PTS	0.91	0.92	0.90	0.90

phantoms. Image matrices of size 256×256 with pixels of size 2.46 mm were acquired in the energy windows W2 and W3.

The scatter-to-total-ratio values were extracted from the result files from the simulation outputs and the primary-to-scatter-ratio (PTS) values were calculated. The values are presented in table 1. The results show that the PTS values vary greatly with patient size. The ^{99m}Tc-to-^{123}I-ratio for PTS, however, varies only slightly with patient size. The average radionuclide ratio for PTS is 0.91 ± 0.01. A penalty term based on this constraint was incorporated into the algorithm. Note that the scatter in this context is the self-scatter from the photopeak in the corresponding photopeak energy window.

The basic ML-EM formula for the problem can be expressed according to equation (6):

$$f_{jb}^{n+1} = \frac{f_{jb}^n}{\sum_{ia} a_{ia,jb}} \cdot \sum_{ia} a_{ia,jb} \cdot \frac{d_{ia}}{\sum_{kc} a_{ia,kc} \cdot f_{kc}^n}, \tag{6}$$

where n is the iteration number. In the context of this work, d_{ia} is the measured counts in the ith energy window of the ath pixel. The quantity f_{jb}^n is the nth estimate of the underlying primary or scatter component in a window (depending on j) for the bth pixel. In the dual-radionuclide problem there are *four* unknowns to be found for *each* pixel. Components $j = 1$ and 2 refer to P_{W2} and S_{W2} and components $j = 3$ and 4 refer to P_{W3} and S_{W3}. The matrix $a_{ia, jb}$ is the system matrix, which couples the jth underlying value in pixel b to the ith measured value in pixel a. Enforcing a prior of the Gibbs-form by the OSL approximation (Green 1990) leads to the following MAP update equation:

$$f_{jb}^{n+1} = \frac{f_{jb}^n}{\sum_{ia} a_{ia,jb} + \beta \frac{\partial U(\mathbf{f})}{\partial f_{jb}} |_{\mathbf{f}=\mathbf{f}^n}} \cdot \sum_{ia} a_{ia,jb} \cdot \frac{d_{ia}}{\sum_{kc} a_{ia,kc} \cdot f_{kc}^n}, \tag{7}$$

where β is the strength with which the prior is enforced and $U(\mathbf{f})$ is the 'energy-function'. A convenient form for the latter quantity, enforcing the observed relationship between the underlying primary and scatter components in the ^{99m}Tc and ^{123}I energy windows, was found to be:

$$U(\mathbf{f}) = \frac{d_{\text{sum}}}{2} \cdot \left(\frac{\sum_b f_{1b}}{\sum_b f_{2b}} - c \cdot \frac{\sum_b f_{3b}}{\sum_b f_{4b}} \right)^2 = \frac{d_{\text{sum}}}{2} \cdot \left(\frac{\sum_b P_{W2}}{\sum_b S_{W2}} - c \cdot \frac{\sum_b P_{W3}}{\sum_b S_{W3}} \right)^2, \tag{8}$$

where $d_{\text{sum}} = \sum_{ia} d_{ia}$ is the total number of measured counts summed over all four energy windows and pixels. Based on the simulations and analysis described above, we have found that to a good approximation $c = 0.91$ (independent of patient size). The final step is to derive the necessary derivatives. These are:

$$\frac{\partial U(\mathbf{f})}{\partial f_{1b}} = d_{\text{sum}} \cdot \frac{1}{\sum\limits_b S_{W2}} \cdot \left(\frac{\sum\limits_b P_{W2}}{\sum\limits_b S_{W2}} - c \cdot \frac{\sum\limits_b P_{W3}}{\sum\limits_b S_{W3}} \right) \tag{9a}$$

$$\frac{\partial U(\mathbf{f})}{\partial f_{2b}} = -d_{\text{sum}} \cdot \frac{\sum\limits_b P_{W2}}{\left(\sum\limits_b S_{W2}\right)^2} \cdot \left(\frac{\sum\limits_b P_{W2}}{\sum\limits_b S_{W2}} - c \cdot \frac{\sum\limits_b P_{W3}}{\sum\limits_b S_{W3}} \right) \tag{9b}$$

$$\frac{\partial U(\mathbf{f})}{\partial f_{3b}} = -c \cdot d_{\text{sum}} \cdot \frac{1}{\sum\limits_b S_{W3}} \cdot \left(\frac{\sum\limits_b P_{W2}}{\sum\limits_b S_{W2}} - c \cdot \frac{\sum\limits_b P_{W3}}{\sum\limits_b S_{W3}} \right) \tag{9c}$$

$$\frac{\partial U(\mathbf{f})}{\partial f_{4b}} = c \cdot d_{\text{sum}} \cdot \frac{\sum\limits_b P_{W3}}{\left(\sum\limits_b S_{W3}\right)^2} \left(\frac{\sum\limits_b P_{W2}}{\sum\limits_b S_{W2}} - c \cdot \frac{\sum\limits_b P_{W3}}{\sum\limits_b S_{W3}} \right). \tag{9d}$$

The purpose of the normalization factor of d_{sum} is now apparent: it removes the scaling of the derivatives with the total number of measured counts. In our numerical studies, a value of $\beta = 0.0045$ has proved successful.

2.5. Phantom studies

Three experimental phantom studies were performed in order to evaluate the obtained images after processing with the proposed algorithm. A thorax phantom (Data Spectrum Corporation, Hillsborough, NC, USA) with a cardiac insert as well as spine- and lung compartments were used. A transaxial slice of a CT-scan of the phantom can be seen in figure 4(*a*). Figures 4(*b*) and (*c*) show the cardiac insert orientated in the vertical long axis and the short axis respectively. Two lesions, as seen in the figures, were included in all three studies. Lesion 1 is fillable and lesion 2 is entirely made of Perspex. In study 1 the myocardium compartment was filled with ^{99m}Tc whilst lesion 1 was filled with non-radioactive water. In study 2 the myocardium compartment and lesion 1 were filled with equal activity concentrations of ^{123}I . In study 3, the dual radionuclide study, the compartments were filled with both ^{99m}Tc and ^{123}I as in studies 1 and 2 (i.e. no ^{99m}Tc in lesion 1). In each study the phantom was scanned ten times in order to estimate the uncertainty on the calculations of lesion contrast. For each scan the acquisition time was increased to account for the decay of ^{99m}Tc.

The count statistics in the phantom study was similar to that of a clinical scan. In the study protocol employed by Ben-Haim *et al* (2014) a 300 MBq injection of ^{99m}Tc-MIBI was followed by a 150 MBq injection of ^{123}I-MIBG approximately 75 min later. The dual radio-nuclide scan started approximately 15 min later with an acquisition time of 20 min. An equivalent ^{99m}Tc activity level of 2.7 MBq for a 20 min scan was used in the experimental studies 1 and 3. With an estimated myocardial uptake of 1.2% for MIBI (Crawford and Husain 2010) this closely corresponds to the ^{99m}Tc activity in the clinical protocol at the time of scan. The equivalent of 2.8 MBq of ^{123}I for a 20 min scan was used in studies 2 and 3. With an estimate of 0.8% for MIBG uptake (Kline *et al* 1981) the level of ^{123}I is elevated compared to the

Table 2. The parameters estimated for use in equations (1) and (2) modelling tailing effects and scatter, respectively.

Photopeak window	Lower window	Tailing parameters		Scatter parameters		
(*ph*)	(*lo*)	$w_{\mathrm{ph}\rightarrow\mathrm{lo}}$	$\sigma_{\mathrm{ph}\rightarrow\mathrm{lo}}$ (cm)	$C_{\mathrm{ph}\rightarrow\mathrm{lo}}$	$\alpha_{\mathrm{ph}\rightarrow\mathrm{lo}}$	$\lambda_{\mathrm{ph}\rightarrow\mathrm{lo}}$ (cm^{-1})
W2	W1	0.422	0.586	0.991	2.442	0.293
W3	W2	0.367	0.588	0.574	1.729	0.373
W3	W1	0.332	0.752	0.938	2.415	0.248

protocol of Ben-Haim *et al*. This poses a worst-case situation with more pollution from ^{123}I to the $^{99\mathrm{m}}$Tc energy window than in the clinical situation.

The D-SPECT list mode data were used to generate projection images for energy windows W1, W2, W3 and W4. The ten scans from study 3 were then processed to extract the primary components (P_{W2} and P_{W3}) using the method described above. Fifteen iterations were used and there was no smoothing applied to the data in the algorithm. The final projection images were normalised by the total expected number of counts in each window and saved. In order to directly compare the results with the images acquired in studies 1 and 2 the following images were also created:

- Contributions from $^{99\mathrm{m}}$Tc in W2 ($P_{\mathrm{W2}} + S_{\mathrm{W2}}$)
- Contributions from ^{123}I in W2 ($P_{\mathrm{W3}\rightarrow\mathrm{W2}} + S_{\mathrm{W3}\rightarrow\mathrm{W2}} + S_{\mathrm{W4}\rightarrow\mathrm{W2}}$)

Tomographic images were reconstructed using an ordered subsets expectation-maximisation (OS-EM) algorithm including collimator response modelling (Spectrum Dynamics). The lesion contrasts in the reconstructed data were calculated using volumes of interest delineated with help from the aligned CT-scan of the phantom as $(a_m - a_l)/a_m$, where a_m and a_l are the average counts in the myocardial and lesion volumes of interest respectively. The coefficient of variation (*CV*) was calculated for the myocardial volume in the $^{99\mathrm{m}}$Tc and $^{99\mathrm{m}}$Tc $+^{123}$I studies for energy window W2 in order to investigate the level of noise.

The count rates (number of detected counts per unit activity per unit time) in the images in W2 from studies 1 and 2 were used to calculate the expected fraction of $^{99\mathrm{m}}$Tc and ^{123}I in W2 in study 3. The results were compared to the fractions obtained after processing using the algorithm.

3. Results

3.1. Parameters for modelling of trapping and Monte Carlo scatter

The values for $w_{\mathrm{ph}\rightarrow\mathrm{lo}}$ and $\sigma_{\mathrm{ph}\rightarrow\mathrm{lo}}$ used in equation (1) for modelling of tailing effects are presented in table 2 together with the values for $C_{\mathrm{ph}\rightarrow\mathrm{lo}}$, $\alpha_{\mathrm{ph}\rightarrow\mathrm{lo}}$ and $\lambda_{\mathrm{ph}\rightarrow\mathrm{lo}}$ used in equation (2) for modelling of scatter. Figure 5 shows normalised line profiles across the images of the capillary tubes for the photopeak energy window as well as the lower energy windows.

Figure 6 shows line profiles across images of the photopeak scatter, the 'true' scatter in the lower window (obtained from the Monte Carlo simulations) and the estimated scatter in the lower window using equation (2). Line profiles are presented for all coupled windows for detector positions 5((*a*)–(*c*)) and 1((*d*)–(*f*)) (with positions and projection angles as presented in figure 1). For illustrative purposes figures 6(*g*) and (*h*) show digitally reconstructed radiographs of the XCAT phantom as seen by these two detectors, with an overlay of the activity

Figure 5. Line profiles across images of the capillary tubes filled with (*a*) ^{99m}Tc in W2 and W1, (*b*) ^{123}I in W3 and W2 and (*c*) ^{123}I in W3 and W1. Gaussian fits to the line profiles are also shown.

distribution. These images were generated by rotating the XCAT attenuation coefficient phantom as well as the activity distribution phantom along the central axis and summing up the 3D-volumes to a planar projection. Figures 6(*i*) and (*j*) show the scatter images in W1 (from ^{99m}Tc) for these two detectors illustrating the positions of the line profiles.

3.2. Phantom study

Figure 7 shows the convergence of estimations of ^{99m}Tc and ^{123}I contributions to W2 as a function of iteration number in the correction algorithm for the first scan of the phantom filled with both radionuclides. Figure 8 shows short axis and vertical long axis views of reconstructed images (with the lesions being oriented in the same way as presented in figure 4) as well as bull's eye plots from all three phantom studies. The images show the mean of the ten scans of each study. Figure 9 shows circular line profiles from the W2 images. The line profiles start at the top of the short axis images (lesion 2) and go all the way around the myocardium.

The obtained lesion contrasts in the three phantom studies are presented in table 3. The distribution of $P_{W2} + S_{W2}$ from the dual radionuclide study (study 3) should be similar to that measured in the single ^{99m}Tc study (study 1) in W2. Note the close corresponding contrasts between these images in table 3. It was also found that the difference in *CV* within the myocardium volume between these two image datasets was very small. This illustrates that no mid-iteration smoothing was necessary to suppress noise at the activity levels investigated.

4. Discussion

The work presented in this study is a continuation on the work by Kacperski *et al* (2011) which was developed for dual radionuclide imaging using ^{99m}Tc and ^{201}Tl . One of the differences is that the estimation of the scatter components in the forward problem in the previous study was used in combination with the triple energy window scatter correction approach. The algorithm presented here directly estimates the scatter components in each energy window and therefore could be considered a more straightforward approach. Another difference is that the parameters for the scatter model were estimated using simulated point sources at various depths in water in the previous study. In this study the parameters were estimated using a digital chest
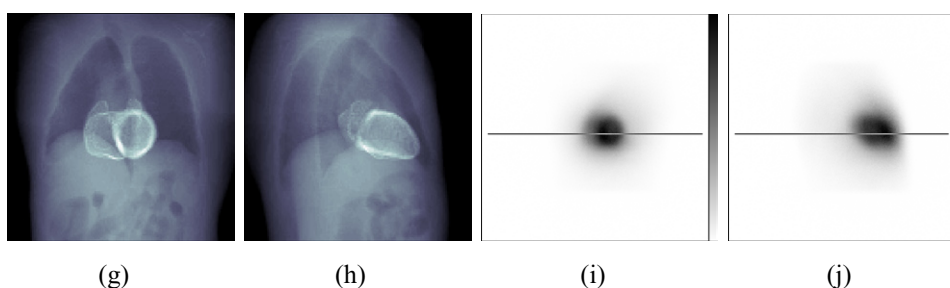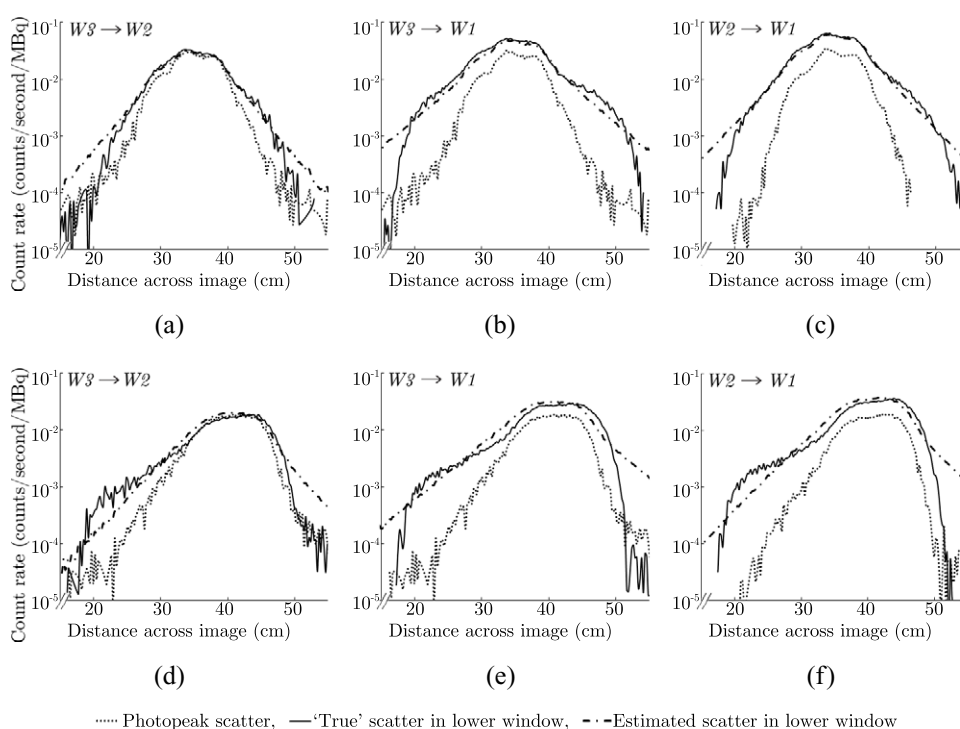
Figure 6. Line profiles across the images of photopeak scatter and lower window scatter obtained from Monte Carlo simulations together with line profiles as estimated in the scatter model for detector 5: (*a*) W3 to W2, (*b*) W3 to W1, (*c*) W2 to W1 and detector 1: (*d*) W3 to W2, (*e*) W3 to W1 and (*f*) W2 to W1. Intensity projections with enhanced heart as seen by detector positions 5 (*g*) and 1 (*h*) and images of the scatter in W1 from ^{99m}Tc with positions of the line profiles for detector positions 5 (*i*) and 1 (*j*).

phantom imaged from the various angles of the D-SPECT detectors. A constraint was incorporated into the ML-EM algorithm to assist convergence in this ^{99m}Tc- and ^{123}I-study.

The line profiles shown in figure 6 show that there is good agreement between the 'true' scatter in a lower energy window (as estimated by Monte Carlo simulations) and that estimated using equation (2) with the parameters presented in table 2. The agreement gets worse towards the edge of the patient as the convolution results in scattered events being placed outside the border of the body outline. This is particularly noticeable in the example shown for detector position 1 from which angle the activity distribution appears near the outline of the body. However, for areas over and near the heart region the agreement is good.
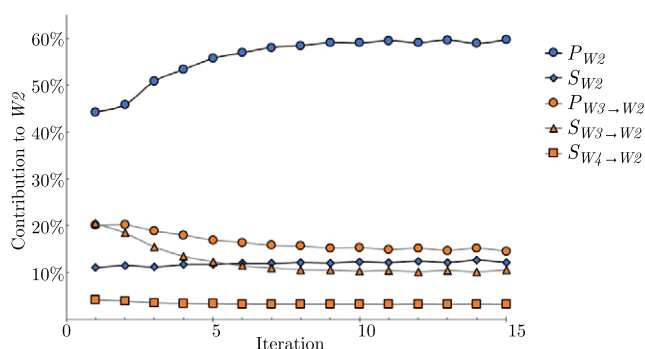
Figure 7. The estimated contributions to W2 as a function of iteration number in the correction algorithm.

It can be seen in figure 8 that there is good spatial agreement in the measured contribution from ^{99m}Tc in W2 in the single radionuclide study (*a*) and that estimated for ^{99m}Tc in W2 in the dual radionuclide study (*f*). There is also good spatial agreement in the measured contribution from ^{123}I in W2 in the single radionuclide study (*b*) and that estimated for ^{123}I in W2 in the dual radionuclide study (*g*). These agreements can also be seen in the line profiles in figure 9, where the magnitude of the correction also can be seen.

The contrast in the estimated contribution from ^{99m}Tc ($P_{W2} + S_{W2}$) in the dual radionuclide study agrees well with that measured in the single ^{99m}Tc study (0.64 ± 0.02 compared to 0.64 ± 0.03 for lesion 1 and 0.75 ± 0.02 compared to 0.80 ± 0.01 for lesion 2). The contrast in the dataset comprised of primary ^{99m}Tc events only, extracted from study 3, has a 20% and 8% improvement in lesion contrast for lesions 1 and 2 respectively compared to the uncorrected dataset. The greatest contrast recovery for ^{99m}Tc is achieved by removing the contributions from ^{123}I . The contrast degradation due to self-scatter for ^{99m}Tc in W2 is only marginal (0.66 ± 0.02 compared to 0.64 ± 0.02 for lesion 1 and 0.78 ± 0.02 compared to 0.75 ± 0.02 for lesion 2). The contrast in the dataset comprised of primary ^{123}I events has a 5% improvement for lesion 2 compared to the uncorrected dataset in W3. Only a small improvement in this energy window (W3) is expected as it is less polluted by extraneous components. The obtained count rates per unit activity in studies 1 and 2 predicted that the fraction of events in W2 originating from ^{99m}Tc and ^{123}I in the first scan of study 3 should be 0.60 and 0.40 respectively. The fractions obtained after processing were found to be 0.71 and 0.29 respectively. This moderate discrepancy would warrant further investigation in future work.

The level of noise in the extracted image $P_{W2} + S_{W2}$ was at the same level as that for the uncorrected image measured in W2 in the single ^{99m}Tc-study. Mid-iteration smoothing of the images was not applied in this study but can be applied to suppress noise (Kacperski *et al* 2011).

The estimation of parameters for the scatter modelling in this study was performed based on a default adult male digital phantom, which is believed to be representative of a typical patient. Whether these parameter fits are sufficiently accurate for unusually large or small patients is worth future investigation. Another subject for future investigation is the impact of excessive extra-cardiac activity on the performance of the proposed correction algorithm.

The obtained images of the primary photopeak counts, which do not have Poisson noise statistics, should strictly speaking not be reconstructed using an ML-EM algorithm, or as in this case, an OS-EM algorithm (Hutton *et al* 2006). However, these initial encouraging results provide a good foundation for future implementation of the model-based correction in the
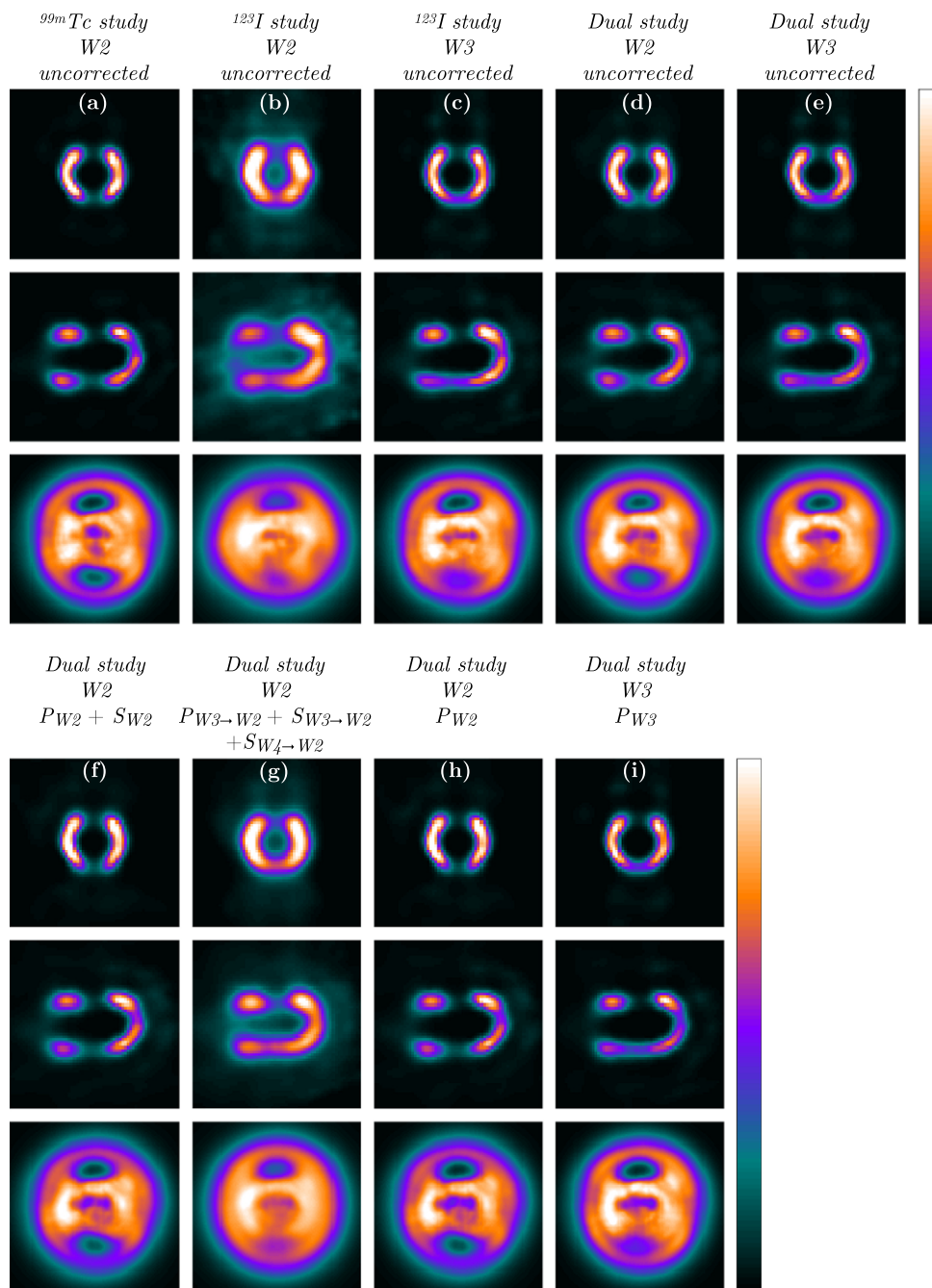
^{99m}Tc study
W2
uncorrected

^{123}I study
W2
uncorrected

^{123}I study
W3
uncorrected

Dual study
W2
uncorrected

Dual study
W3
uncorrected

Dual study
W2
$P_{W2} + S_{W2}$

Dual study
W2
$P_{W3 \to W2} + S_{W3 \to W2}$
$+ S_{W4 \to W2}$

Dual study
W2
P_{W2}

Dual study
W3
P_{W3}

Figure 8. The obtained images in the reconstructed data from the uncorrected images from studies 1 (^{99m}Tc), 2 (^{123}I) and 3 (^{99m}Tc and ^{123}I) as well as the reconstructed data from the estimated contributions after processing study 3.

reconstruction software via the use of the extracted projections of primary counts. An alternative approach, preserving Poisson statistics, would be to explore the addition of the estimated
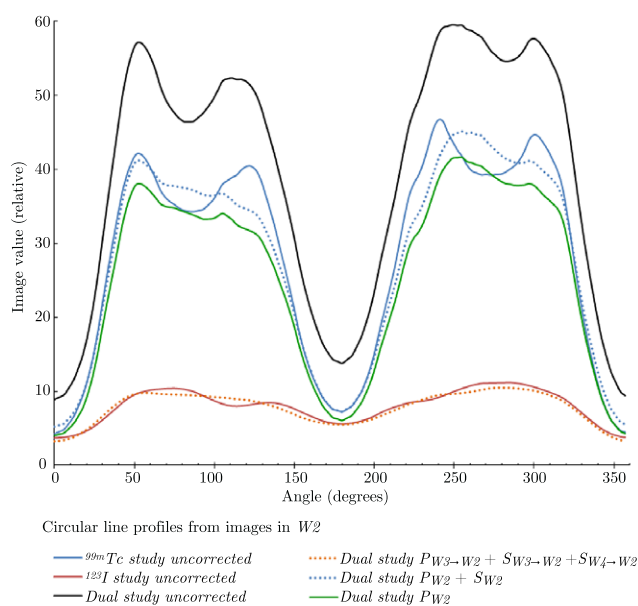
Circular line profiles from images in *W2*

- —— ^{99m}Tc *study uncorrected*
- —— ^{123}I *study uncorrected*
- —— *Dual study uncorrected*
- ⋯⋯ *Dual study* $P_{W3 \to W2} + S_{W3 \to W2} + S_{W4 \to W2}$
- ⋯⋯ *Dual study* $P_{W2} + S_{W2}$
- —— *Dual study* P_{W2}

Figure 9. Circular line profiles from short axis slices of the obtained data from the uncorrected images in W2 from studies 1 (^{99m}Tc), 2 (^{123}I) and 3 (^{99m}Tc and ^{123}I) as well as the estimated contributions after processing study 3.

Table 3. The obtained lesion contrasts in the reconstructed data from the uncorrected images from studies 1 (^{99m}Tc), 2 (^{123}I) and 3 (^{99m}Tc and ^{123}I) as well as the estimated contributions after processing study 3.

Study	Window	Data[a]	Lesion contrast[b]		CV[d,e]
			Lesion 1[c]	Lesion 2	
1 (^{99m}Tc)					
	W2	uncorrected (a)	0.64 ± 0.02	0.80 ± 0.01	$52\% \pm 1\%$
2 (^{123}I)					
	W2	uncorrected (b)	0.21 ± 0.06	0.50 ± 0.04	$35\% \pm 1\%$
	W3	uncorrected (c)	—	0.76 ± 0.02	$49\% \pm 1\%$
3 (^{99m}Tc & ^{123}I)					
	W2	uncorrected (d)	0.55 ± 0.01	0.72 ± 0.01	$43\% \pm 1\%$
	W2	$P_{W2} + S_{W2}(f)$	0.64 ± 0.02	0.75 ± 0.02	$50\% \pm 1\%$
	W2	$P_{W2}(h)$	0.66 ± 0.02	0.78 ± 0.02	$54\% \pm 1\%$
	W2	$P_{W3 \to W2} + S_{W3 \to W2} + S_{W4 \to W2}(g)$	0.18 ± 0.02	0.54 ± 0.01	$28\% \pm 1\%$
	W3	uncorrected (e)	—	0.76 ± 0.01	$48\% \pm 1\%$
	W3	$P_{W3}(i)$	—	0.80 ± 0.01	$54\% \pm 1\%$

[a] The letter in parentheses indicate the position in figure 8.
[b] The values presented are mean ± standard deviation for the ten scans.
[c] Lesion 1 was only a defect (cold) for the ^{99m}Tc-distribution.
[d] Coefficient of variation in the myocardial volume of interest.
[e] The values presented are mean ± standard deviation for the ten scans.

scatter projections to the forward projections within the iterative reconstruction, as discussed in Hutton *et al* (2011).

5. Conclusion

We have developed a model-based iterative algorithm to correct for in-patient scatter and tailing effects in dual radionuclide imaging with ^{99m}Tc and ^{123}I for a CdZnTe-detector cardiac camera. Parameters for the modelling of scatter were simulated using the Monte Carlo technique and parameters for the modelling of tailing effects were estimated using experimental measurements. The algorithm yielded improved images for both ^{99m}Tc and ^{123}I with increased lesion contrast.

Acknowledgments

References

Baggish A L and Boucher C A 2008 Radiopharmaceutical agents for myocardial perfusion imaging *Circulation* **118** 1668–74

Ben-Haim S, Menichetti F, Allie R, Roth N, Baavour R, Rubens M, Bomanji J, Underwood S and Ernst S 2014 Simultaneous dual-radionuclide imaging with ^{99m} Technetium-MIBI and ^{123} I-mIBG in patients with ventricular arrhythmia—initial experience *J. Nucl. Med.* **55** 1723 (Suppl. 1)

Ben-Haim S *et al* 2013 Quantification of myocardial perfusion reserve using dynamic SPECT imaging in humans: a feasibility study *J. Nucl. Med.* **54** 873–9

Chirumamilla A and Travin M I 2011 Cardiac applications of 123I-mIBG imaging *Semin. Nucl. Med.* **41** 374–87

Crawford E S, Husain S S 2010 Radiopharmaceuticals *Nuclear Cardial Imaging: Terminology and Technical Aspects* ed E S Crawford and S S Husain vol 11 (Reston, VA: Society of Nuclear Medicine)

De Geeter F, Franken P R, Knapp F F and Bossuyt A 1994 Relationship between blood flow and fatty acid metabolism in subacute myocardial infarction: a study by means of ^{99m} Tc-Sestamibi and ^{123} I-beta-methyl-iodo-phenyl pentadecanoic acid *Eur. J. Nucl. Med.* **21** 283–91

de Jong H W A M and Beekman F J 2000 Efficient photon cross-talk calculation in SPECT *IEEE Nucl. Sci. Symp. Conf. Rec.* **2** 13 /30–4

Devous M D, Lowe J L and Payne J K 1992 Dual-isotope brain SPECT imaging with technetium-99m and iodine-123: validation by phantom studies *J. Nucl. Med.* **33** 2030–5

El Fakhri G, Habert M O, Maksud P, Kas A, Malek Z, Kijewski M F and Lacomblez L 2006 Quantitative simultaneous ^{99m} Tc-ECD/^{123} I-FP-CIT SPECT in Parkinsons disease and multiple system atrophy *Eur. J. Nucl. Med. Mol. Imag.* **33** 87–92

El Fakhri G, Maksud P, Kijewski M F, Zimmerman R E and Moore S C 2002 Quantitative simultaneous ^{99m} Tc/^{123} I SPECT: design study and validation with Monte Carlo simulations and physical acquisitions *IEEE Trans. Nucl. Sci.* **49** 2315–21

El Fakhri G, Moore S C, Maksud P, Aurengo A and Kijewski M F 2001 Absolute activity quantitation in simultaneous ^{123} I/^{99m} Tc brain SPECT *J. Nucl. Med.* **42** 300–8

El Fakhri G, Sitek A, Zimmerman R E and Ouyang J 2006 Generalized five-dimensional dynamic and spectral factor analysis *Med. Phys.* **33** 1016–24

El Fakhri G, Maksud P, Kijewski M F, Habert M O, Todd-Pokropek A, Aurengo A and Moore S C 2000 Scatter and cross-talk corrections in simultaneous Tc-99m/I-123 brain SPECT using constrained factor analysis and artificial neural networks *IEEE Trans. Nucl. Sci.* **47** 1573–80

Erlandsson K, Kacperski K, van Gramberg D and Hutton B F 2009 Performance evaluation of D-SPECT: a novel SPECT system for nuclear cardiology *Phys. Med. Biol.* **54** 2635–49

Gimelli A, Bottai M, Giorgetti A, Genovesi D, Filidei E and Marzullo P 2012 Evaluation of ischaemia in obese patients: feasibility and accuracy of a low-dose protocol with a cadmium-zinc telluride camera *Eur. J. Nucl. Med. Mol. Imag.* **39** 1254–61

Green P J 1990 Bayesian reconstructions from emission tomography data using a modified EM algorithm *IEEE Trans. Med. Imag.* **9** 84–93

Hapdey S, Soret M and Buvat I 2006 Quantification in simultaneous ^{99m}Tc/^{123}I brain SPECT using generalized spectral factor analysis: a Monte Carlo study *Phys. Med. Biol.* **51** 6157–71

Hindié E, Mellière D, Jeanguillaume C, Perlemuter L, Chéhadé F and Galle P 1998 Parathyroid imaging using simultaneous double-window recording of technetium-99m-sestamibi and iodine-123 *J. Nucl. Med.* **39** 1100–5

Hutton B F, Buvat I and Beekman F J 2011 Review and current status of SPECT scatter correction *Phys. Med. Biol.* **56** R85–112

Hutton B F, Nuyts J and Zaidi H 2006 Iterative reconstruction methods *Quantitative Analysis in Nuclear Medicine Imaging* ed H Zaidi (Berlin: Springer) pp 126–8

Ivanovic M and Weber D A 1994 Feasibility of dual radionuclide brain imaging with I-123 and Tc-99m *Med. Phys.* **21** 667–74

Kacperski K, Erlandsson K, Ben-Haim S and Hutton B F 2011 Iterative deconvolution of simultaneous ^{99m}Tc and ^{201}Tl projection data measured on a CdZnTe-based cardiac SPECT scanner *Phys. Med. Biol.* **56** 1397–414

Kadrmas D J, Frey E C and Tsui B M 1999 Simultaneous technetium-99m/thallium-201 SPECT imaging with model-based compensation for cross-contaminating effects *Phys. Med. Biol.* **44** 1843–60

Kline R C, Swanson D P, Wieland D M, Thrall J H, Gross M D, Pitt B and Beierwaltes W H 1981 Myocardial imaging in man with I-123 Meta-Iodobenzylguanidine *J. Nucl. Med.* **22** 129–32 (PMID: 7463156)

Kobayashi H, Momose M, Kanaya S, Kondo C, Kusakabe K and Mitsuhashi N 2003 Scatter correction by two-window method standardizes cardiac I-123 MIBG uptake in various gamma camera systems *Ann. Nucl. Med.* **17** 309–13

Kumita S *et al* 2000 Simultaneous assessment of Tc-99m-sestamibi and I-123-BMIPP myocardial distribution in patients with myocardial infarction: evaluation of left ventricular function with ECG-gated myocardial SPECT *Ann. Nucl. Med.* **14** 453–9

Leo W R 1994 *Techniques for Nuclear and Particle Physics Experiments* 2nd edn (Berlin: Springer)

Ljungberg M, Liu C, Fan P and Pretorius H 2014 Monte Carlo simulations of the GE Discovery Alcyone CZT SPECT system *Nucl. Sci. Symp. Medical Imaging Conf.* (*NSS/MIC*) (Piscataway, NJ: IEEE)

Ljungberg M and Strand S-E 1989 A Monte Carlo program for the simulation of scintillation camera characteristics *Comput. Methods Prog. Biomed.* **29** 257–72

MATLAB and Global Optimization Toolbox Release 2013a, 2013 *Computer Software* (Natick: The MathWorks)

Meikle S R, Hutton B F, Bailey D L, Fulton R R, Schindhelm K 1991 *Information Processing in Medical Imaging* Colchester A C F and Hawkes D S (Berlin: Springer) pp 34–44

Muxi A, Magrina J, Martín F, Josa M, Fuster D, Setoain F J, Perez-Villa F, Pavia J and Bosch X 2003 Technetium 99m-labeled tetrofosmin and iodine 123-labeled metaiodobenzylguanidine scintigraphy in the assessment of transmyocardial laser revascularization *J. Thorac. Cardiovasc. Surg.* **125** 1493–8

Nakazato R, Berman D S, Hayes S W, Fish M, Padgett R, Xu Y, Lemley M, Baavour R, Roth N and Slomka P J 2013 Myocardial perfusion imaging with a solid-state camera: simulation of a very low dose imaging protocol *J. Nucl. Med.* **54** 373–9

National Nuclear Data Center (NNDC) 2000 ENSDF Decay Data in the MIRD (Medical Internal Radiation Dose) Format for 123I (www.orau.org/PTP/PTP%20Library/library/DOE/bnl/nuclidedata/MIRI123.htm)

Ogawa K, Harata Y, Ichihara T, Kubo A and Hashimoto S 1991 A practical method for position-dependent Compton scatter correction in single photon emission CT *IEEE Trans. Med. Imaging* **10** 408–12

Ouyang J, El Fakhri G and Moore S C 2007 Fast Monte Carlo based joint iterative reconstruction for simultaneous ^{99m}Tc/^{123}I SPECT imaging *Med. Phys.* **34** 3263–72

Ouyang J, Zhu X, Trott C M and El Fakhri G 2009 Quantitative simultaneous [99m] Tc/[123] I cardiac SPECT using MC-JOSEM *Med. Phys.* **36** 602–11

Segars W P, Sturgeon G, Mendonca S, Grimes J and Tsui B M 2010 4D XCAT phantom for multimodality imaging research *Med. Phys.* **37** 4902–15

Shcherbinin S, Celler A, Trummer M and Humphries T 2009 An APD-based iterative reconstruction method for simultaneous technetium-99m/iodine-123 SPECT imaging *Phys. Med.* **25** 192–200

Verani M S, Taillefer R, Iskandrian A E, Mahmarian J J, He Z X and Orlandi C 2000 [123] I-IPPA SPECT for the prediction of enhanced left ventricular function after coronary bypass graft surgery. Multicenter IPPA viability trial investigators. ^{123}I-iodophenylpentadecanoic acid *J. Nucl. Med.* **41** 1299–307

Wagenaar D J 2004 CdTe and CdZnTe semiconductor detectors for nuclear medicine imaging *Emission Tomography: the Fundamentals of PET and SPECT* ed M N Wernick and J N Aarsvold (London: Elsevier) pp 276–9

Zheng X M, Zubal I G, Seibyl J P and King M A 2004 Correction for cross-talk contamination in dual radionuclide [99m] Tc and [123] I images using artificial neural network *IEEE Trans. Nucl. Sci.* **51** 2649–53